



Research Paper

Buckling Behavior of Nanocomposite Plates with Functionally Graded Properties under Compressive Loads in Elastic and Thermal Environments

Cengiz Ipek¹, Abdullah H. Sofiyev^{2,3}, Nicholas Fantuzzi⁴, Sadige P. Efendiyeva⁵

¹ Department of Civil Engineering, Engineering Faculty, Istanbul Medeniyet University, Istanbul 34700, Turkey, Email: cengiz.ipek@medeniyet.edu.tr

² Department of Mathematics, Istanbul Ticaret University, Beyoglu 34445/Istanbul, Turkey, Email: aavey@ticaret.edu.tr

³ Scientific Research Centers for Composition Materials of UNEC Azerbaijan State Economic University, Baku 1001, Azerbaijan

⁴ Department of Civil, Chemical, Environmental, and Materials Engineering, University Bologna, Italy, Email: nicholas.fantuzzi@unibo.it

⁵ Department of Radio-electronics and Aerospace Systems, Azerbaijan Technical University, Baku 1001, Azerbaijan, Email: esadiqa@mail.ru

Received February 20 2023; Revised March 22 2023; Accepted for publication March 26 2023.

Corresponding author: A.H. Sofiyev (aavey@ticaret.edu.tr)

© 2023 Published by Shahid Chamran University of Ahvaz

Abstract. The buckling behavior of functionally graded carbon nanotube (FG-CNT) reinforced polymer-based moderately-thick plates subjected to in-plane biaxial compressive loads in elastic and thermal environments in the framework of first-order shear deformation plate theory (FSDPT) is investigated. First, the temperature-dependent properties of CNTs and nanocomposites are defined and their constitutive relations are established, then the stability and strain compatibility equations in elastic media are derived in the framework of the FSDPT. Then, by applying the Galerkin method to the basic equations, a closed-form solution is obtained for the critical biaxial compressive loads. The specific numerical analyzes and interpretations are made for various plate sizes and CNT patterns on the Winkler elastic foundation and in thermal environments within FSDPT and classical plate theory (CPT).

Keywords: Moderately-thick plate, nanocomposite, functionally graded, in-plane biaxial loads, buckling, elastic foundations.

1. Introduction

Among the nanomaterials used to create nanocomposites with superior mechanical and functional properties, which have the potential for a wide variety of industrial applications, carbon nanotubes (CNTs) maintain their leading role as reinforcement elements today [1]. Due to their unique structural properties that provide high chemical and thermal stability, CNTs have an important place in obtaining advanced engineering materials [2, 3]. The extraordinary electrical and thermal conductivity of CNTs as well as surface modification capabilities make it more attractive to be applied as a reinforcement element [4, 5]. Recent research reveals that CNTs are particularly suitable for the production of advanced electrically conductive polymer composites [6].

Reinforcing polymers using fillers, whether inorganic or organic, is common in the production of modern plastics, and polymeric nanocomposites represent a serious alternative to traditional filled polymers or polymer blends. Polymeric nanocomposites are classified as nanoclay reinforced polymer-based composites, carbon nanotube reinforced polymer composites, nanofiber reinforced polymer composites and inorganic particle reinforced polymer composites. Among polymer-based composites, carbon nanotube reinforced polymer composites have the most application potential. In recent years, polymer-based nanocomposites are frequently used in many engineering branches and industries that use new technology, including the defense industry. The applications of polymer nanocomposites are very diverse, and their significant impact on the automotive industry can be highlighted, including in tires, fuel systems, fuel cells and seat textiles, gas separation membranes, mirror housings in various vehicle types, door handles, engine covers. When polymer-based nanocomposites are used as the main structural element, it is noteworthy that more plate-shaped elements are used. The initiative in this area, which started with the work of Shen [7], led to the emergence of many studies on the thermo-mechanical stability and vibration behavior of plates made of polymer nanocomposites [8-28]. In recent years, the use of polymer-based nanocomposite plates in various environments, especially in elastic and thermal environments, necessitates updating their stability and vibration behavior during design. The first studies on this subject were carried out with the initiatives of Liew and his colleagues [29], and the number of studies in this field has increased in terms of quality and quantity in recent years [30-39].

The review of the literature reveals that the problem of buckling of moderately-thick nanocomposite plates in elastic and thermal environments subjected to in-plane biaxial compressive loads in FSDPT has not been adequately investigated



analytically. In this study, this issue is discussed in detail. The organization of the paper is as follows: Section 2 describes the temperature dependent properties of moderately-thick thickness nanocomposite plates and the Winkler base. In Section 3, the fundamental relationships are established for nanocomposite plates on the Winkler foundation and then stability equations are derived in the framework of the FSDPT. In Section 4, the closed-form solution for the critical biaxial compressive load is obtained. After checking the accuracy of the expressions obtained in Section 5, the specific analysis and interpretation are performed for various plate sizes and CNT structures, in elastic and thermal environments, within FSDPT and CPT.

2. Theoretical Developments

2.1 Formulation of the problem

The moderately-thick rectangular plate with CNT reinforcement with side lengths a and b , and the thickness h , respectively, resting on the Winkler elastic foundation and subjected in-plane biaxial forces and Oxyz coordinate system are illustrated in Fig. 1. The displacements of the nanocomposite plate along the x, y and z axes are assumed to be u, v, w , respectively, whose material properties depend on location (z_1) and temperature (T). The domain of the plate is defined as:

$$\Lambda = \{x, y, z : (x, y, z) \in [0, a] \times [0, b] \times [-h/2, h/2]\} \tag{1}$$

The nanocomposite plate is resting on the elastic foundation whose supporting action is described by the Winkler model, as $R = K_w w$ in which R represent the foundation reaction per unit area, and K_w represent coefficients of the spring layer or Winkler elastic foundation.

2.2. Modeling of nanocomposites

Assuming that the material properties of CNTs and matrix, which are the components of the nanocomposite plate, are temperature dependent, the effective elastic properties of nanocomposites can be written as follows [7]:

$$Y_{11}(z_1, T) = \eta_1 V_{cnt}^{z_1} Y_{11}^{cnt}(T) + V_m Y_m(T), \quad \frac{\eta_2}{Y_{22}(z_1, T)} = \frac{V_{cnt}^{z_1}}{Y_{22}^{cnt}(T)} + \frac{V_m}{Y_m(T)}, \quad \frac{\eta_3}{Y_{12}(z_1, T)} = \frac{V_{cnt}^{z_1}}{Y_{12}^{cnt}(T)} + \frac{V_m}{Y_m(T)}, \tag{2}$$

$$Y_{13}(z_1, T) = Y_{12}(z_1, T), \quad Y_{23}(z_1, T) = 1.2 Y_{12}(z_1, T), \quad \nu_{12} = V_{cnt}^{z_1} \nu_{12}^{cnt} + V_m \nu^m, \quad \rho = V_{cnt}^{z_1} \rho^{cnt} + V_m \rho^m, \quad z_1 = z/h$$

and the coefficients of thermal expansion are expressed as:

$$\alpha_{11}(z_1, T) = \frac{\alpha_{11}^{cnt} V_{cnt}^{z_1} Y_{12}^{cnt}(T) + V_m Y_m(T) \alpha_m}{V_{cnt}^{z_1} Y_{11}^{cnt}(T) + V_m Y_m(T)}, \tag{3}$$

$$\alpha_{22}(z_1, T) = (1 + \nu_{12}^{cnt}) \alpha_{22}^{cnt} V_{cnt}^{z_1} + (1 + \nu_m) V_m \alpha_m - \nu_{12}^{cnt} \alpha_{11}(z_1, T)$$

where $Y_{ij}^{cnt}(T)$, ($i = 1, 2; j = 1, 2, 3$) and $Y_m(T)$ represent the Young and shear moduli, ρ^{cnt} and ρ^m represent densities, ν_{12}^{cnt} and ν_{12}^m represent Poisson ratios, α_{11}^{cnt} and α_m designate thermal expansion coefficients of CNT and polymer matrix. The efficiency parameters of CNT are designated as η_j ($j = 1, 2, 3$). The volume fraction of CNTs and matrix material are designated as $V_{cnt}^{z_1}$ and V_m in which $V_{cnt}^{z_1} + V_m = 1$. Also, the carbon nanotube ratio are found from the expression [7-9]:

$$V_{cnt}^{z_1} = \frac{m_{cnt}}{m_{cnt} + (\rho^{cnt} / \rho^m)(1 - m_{cnt})} \tag{4}$$

where m_{cnt} stands for the mass fraction of CNT in the nanocomposite material. The four types of patterns are considered in this study, i.e., UD, VD, OD and XD. The expression for $V_{cnt}^{z_1}$ are given in Table 1.

The geometric modeling of the profiles presented in Table 1, in other words, the cross-sections of the nanocomposite plate with profiles (a) UD, (b) VD, (c) OD and (d) XD are illustrated in Fig. 2.

Table 1. Pattern types of CNTs in the matrix.

Pattern types	UD	AD	VD	OD	XD
$V_{cnt}^{z_1}$	$V_{cnt}^{z_1}$	$(1 + 2z_1) V_{cnt}^{z_1}$	$(1 - 2z_1) V_{cnt}^{z_1}$	$2(1 - 2 z_1) V_{cnt}^{z_1}$	$4 z_1 V_{cnt}^{z_1}$

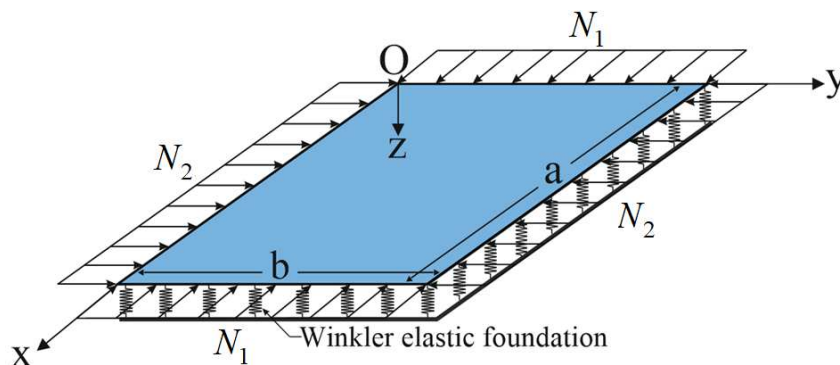


Fig. 1. CNT-patterned polymer rectangular plate under biaxial compressive loads.



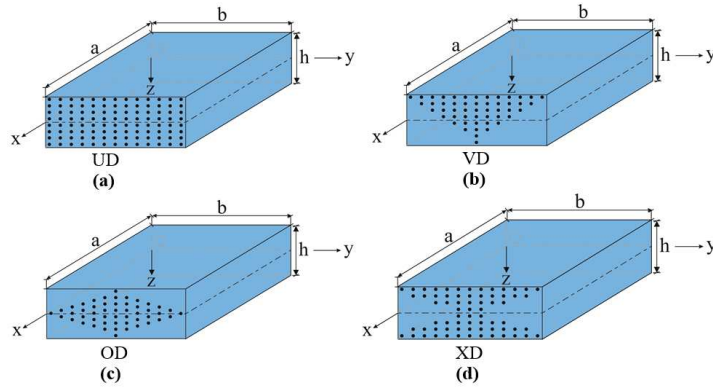


Fig. 2. Cross-sections of rectangular plates with CNT-profiles (a) UD, (b) VD, (c) OD and (d) XD.

3. Fundamental Relations and Equations

Considering the assumption of transverse shear deformations, the relationships between τ_{ij} stresses and ϵ_{ij} ($i = 1, 2; j = 1, 2, 3$) strains of plates made of nanocomposites are expressed as follows [7]:

$$\begin{bmatrix} \tau_{11} \\ \tau_{22} \\ \tau_{12} \end{bmatrix} = \begin{bmatrix} Q_{11}(z_1, T) & Q_{12}(z_1, T) & 0 \\ Q_{21}(z_1, T) & Q_{22}(z_1, T) & 0 \\ 0 & 0 & Q_{66}(z_1, T) \end{bmatrix} \begin{bmatrix} \epsilon_{11} \\ \epsilon_{22} \\ \epsilon_{12} \end{bmatrix} + \begin{bmatrix} \tau_{11T} \\ \tau_{22T} \\ 0 \end{bmatrix} \quad (5)$$

and

$$\begin{bmatrix} \tau_{13} \\ \tau_{23} \end{bmatrix} = \begin{bmatrix} Q_{55}(z_1, T) & 0 \\ 0 & Q_{44}(z_1, T) \end{bmatrix} \begin{bmatrix} \epsilon_{13} \\ \epsilon_{23} \end{bmatrix} \quad (6)$$

where

$$\begin{aligned} Q_{11}(z_1, T) &= \frac{Y_{11}(z_1, T)}{1 - \nu_{12}\nu_{21}}, & Q_{12}(z_1, T) &= \frac{\nu_{21}Y_{11}(z_1, T)}{1 - \nu_{12}\nu_{21}} = \frac{\nu_{12}Y_{22}(z_1, T)}{1 - \nu_{12}\nu_{21}} = Q_{21}(z_1, T), & Q_{22}(z_1, T) &= \frac{Y_{22}(z_1, T)}{1 - \nu_{12}\nu_{21}}, \\ Q_{66}(z_1, T) &= Y_{12}(z_1, T), & Q_{55}(z_1, T) &= Y_{23}(z_1, T), & Q_{44}(z_1, T) &= Y_{23}(z_1, T) \end{aligned} \quad (7)$$

The thermal stress components, τ_{iT} ($i = 1, 2$) are expressed as follows [41]:

$$\begin{bmatrix} \tau_{11}^T \\ \tau_{22}^T \end{bmatrix} = \begin{bmatrix} Q_{11}(z_1, T), & Q_{12}(z_1, T) \\ Q_{21}(z_1, T), & Q_{22}(z_1, T) \end{bmatrix} \begin{bmatrix} \alpha_{11}(z_1, T) \\ \alpha_{22}(z_1, T) \end{bmatrix} \Delta T \quad (8)$$

where ΔT is the uniform temperature rise from the reference temperature ($T_0 = 300$ K in room temperature) at which the plate is free of thermal stresses.

When the assumptions proposed in Ref. [40] are modified to functionally graded nanocomposites, the following relations can be rewritten:

$$[\epsilon_{13}, \epsilon_{23}] = \left[\frac{f_1(x, y)}{G_{13}(z_1, T)} \frac{d\Gamma(z)}{dz}, \frac{f_2(x, y)}{G_{23}(z_1, T)} \frac{d\Gamma(z)}{dz} \right] \quad (9)$$

where, the $\Gamma(z)$ function is the function characterizing the transverse shear stresses τ_{13} and τ_{23} , G_{13} and G_{23} are the shape functions depending on the thickness coordinate of the plate, $f_1(x, y)$ and $f_2(x, y)$ are functions of rotation angles.

Using the expressions (5), (6), (8) and (9) together, the strain components at any point in the plate thickness ($\epsilon_{11}, \epsilon_{22}, \gamma_{12}$) with those of mid-plane ($\epsilon_{011}, \epsilon_{022}, \gamma_{012}$) can be expressed as follows:

$$\begin{bmatrix} \epsilon_{11} \\ \epsilon_{22} \\ \gamma_{12} \end{bmatrix} = \begin{bmatrix} \epsilon_{011} - z \frac{\partial^2 w}{\partial x^2} \\ \epsilon_{022} - z \frac{\partial^2 w}{\partial y^2} \\ \gamma_{012} - 2z \frac{\partial^2 w}{\partial x \partial y} \end{bmatrix} + \begin{bmatrix} \delta_1(z, T) \frac{\partial f_1}{\partial x} \\ \delta_2(z, T) \frac{\partial f_2}{\partial y} \\ \delta_1(z, T) \frac{\partial f_1}{\partial y} + \delta_2(z, T) \frac{\partial f_2}{\partial x} \end{bmatrix} \quad (10)$$

The following definitions apply in this relation:

$$\delta_1(z, T) = \int_0^z \frac{1}{G_{13}(z_1, T)} \frac{d\Gamma(z)}{dz} dz, \quad \delta_2(z) = \int_0^z \frac{1}{G_{23}(z_1, T)} \frac{d\Gamma(z)}{dz} dz \quad (11)$$

To find the in-plane force and moment components N_{ij} ($i, j = 1, 2$) and M_{ij} ($i, j = 1, 2$), and the transverse shear forces Q_i ($i = 1, 2$), the stress components defined by (5) and (6) are integrated from $-h/2$ to $+h/2$ depending on the thickness coordinate, z [40]:



$$[N_{ij}, M_{ij}] = \int_{-h/2}^{h/2} \tau_{ij}[1, z] dz + [N_{ii}^T, M_{ii}^T], \quad (i, j = 1, 2), \quad [Q_1, Q_2] = \int_{-h/2}^{h/2} [\tau_{13}, \tau_{23}] dz \quad (12)$$

where the force and moment components of thermal stresses $N_{ii}^T (i = 1, 2)$ and $M_{ii}^T (i = 1, 2)$ are found from the following integrals [7, 41]:

$$\begin{bmatrix} N_{11}^T & M_{11}^T \\ N_{22}^T & M_{22}^T \end{bmatrix} = \int_{-h/2}^{h/2} \begin{bmatrix} \tau_{11}^T \\ \tau_{22}^T \end{bmatrix} [1, z] dz \quad (13)$$

The correlation between the forces $N_{ij} (i, j = 1, 2)$ and stress function F is determined as follows [40-43]:

$$[N_{11}, N_{22}, N_{12}] = h \left[\frac{\partial^2 F}{\partial x^2}, \frac{\partial^2 F}{\partial y^2}, -\frac{\partial^2 F}{\partial x \partial y} \right] \quad (14)$$

Within the FSDPT, the general stability equations of plates subjected to in-plane compressive loads are expressed as follows [40-43]:

$$\frac{\partial M_{11}}{\partial x} + \frac{\partial M_{12}}{\partial y} - Q_1 = 0, \quad \frac{\partial M_{21}}{\partial x} + \frac{\partial M_{22}}{\partial y} - Q_2 = 0, \quad \frac{\partial Q_1}{\partial x} + \frac{\partial Q_2}{\partial y} - N_1 \frac{\partial^2 w}{\partial x^2} - N_2 \frac{\partial^2 w}{\partial y^2} + k_1 w = 0 \quad (15)$$

where N_1 and N_2 are the compressive loads in the x and y directions.

It is known that the deformation compatibility equation of the plate is expressed as follows [37]:

$$\frac{\partial^2 \varepsilon_{011}}{\partial y^2} + \frac{\partial^2 \varepsilon_{022}}{\partial x^2} - \frac{\partial^2 \gamma_{012}}{\partial x \partial y} = 0 \quad (16)$$

By using Eqs. (5), (10), (12) and (13) together with the relation (14), the force and moment components and additionally the deformations in the mid-plane are expressed with four functions, namely, transverse deflection, rotation angles and Airy stress functions, and the resulting expressions substituted in the basic equations (15) and (16), one gets:

$$\begin{aligned} L_{11}F + L_{12}w + L_{13}f_1 + L_{14}f_2 &= 0 \\ L_{21}F + L_{22}w + L_{23}f_1 + L_{24}f_2 &= 0 \\ L_{31}F + L_{32}w + L_{33}f_1 + L_{34}f_2 &= 0 \\ L_{41}F + L_{42}w + L_{43}f_1 + L_{44}f_2 &= 0 \end{aligned} \quad (17)$$

where L_{ij} are differential operators and defined in Appendix A.

In order to demonstrate the advantages of the shear deformation theory, it is necessary to derive the stability equation of the nanocomposite plate subjected to the in-plane compressive loads, also within the framework of the classical shell theory. As it is known that when CST is used, the above four equations turn into two equations, in other words, the deformation compatibility equation, that is, the Eq. (16) remains the same in appearance, while set of Eqs. (15) turn into the following equation [40, 41]:

$$\frac{\partial^2 M_{11}}{\partial x^2} + 2 \frac{\partial^2 M_{12}}{\partial x \partial y} + \frac{\partial^2 M_{22}}{\partial y^2} - N_1 \frac{\partial^2 w}{\partial x^2} - N_2 \frac{\partial^2 w}{\partial y^2} + k_1 w = 0 \quad (18)$$

If transverse shear strains, i.e. (6) are not taken into account, continuing a similar procedure, the moment and strain components in the mid-plane can be expressed in terms of the deflection and stress functions, and then substituting them into (16) and (18), the basic equations in the framework of CST take the following form:

$$\begin{aligned} \mathcal{L}_{11}F + \mathcal{L}_{12}w_2 &= 0 \\ \mathcal{L}_{21}F + \mathcal{L}_{22}w &= 0 \end{aligned} \quad (19)$$

where \mathcal{L}_{ij} are differential operators and defined in Appendix B.

4. Solution Method

Simply supported boundary conditions are taken into account to solve the basic differential equations derived from the previous section, which contain the properties of the plate composed of FG-CNT-patterned material.

$$w = M_{11} = \frac{\partial^2 F}{\partial y^2} = 0, \quad \text{if } x = 0 \text{ and } a; \quad w = M_{22} = \frac{\partial^2 F}{\partial x^2} = 0, \quad \text{if } y = 0 \text{ and } b \quad (20)$$

The solution of the differential equations (17) satisfying the boundary conditions (20) is sought as follows [37-39]:

$$\begin{aligned} F &= \sum_{m=1}^{\infty} \sum_{n=1}^{\infty} C_{mn}^F \sin(px) \sin(qy), \quad w = \sum_{m=1}^{\infty} \sum_{n=1}^{\infty} C_{mn}^w \sin(px) \sin(qy), \\ f_1 &= \sum_{m=1}^{\infty} \sum_{n=1}^{\infty} C_{mn}^{f_1} \cos(px) \sin(qy), \quad f_2 = \sum_{m=1}^{\infty} \sum_{n=1}^{\infty} C_{mn}^{f_2} \sin(px) \cos(qy) \end{aligned} \quad (21)$$

where the terms $C_{mn}^F, C_{mn}^w, C_{mn}^{f_1}, C_{mn}^{f_2}$ are unknown coefficients to be determined, $p = m\pi/a$ and $q = n\pi/b$ are parameters and the (m, n) is the buckling mode.

When (21) are substituted in the system of Eqs. (17) and the Galerkin method is applied, the following 4×4 matrix equation is obtained:



$$\begin{bmatrix} r_{11} & -r_{12} & r_{13} & r_{14} \\ r_{21} & -r_{22} & r_{23} & r_{24} \\ r_{31} & -r_{32} & r_{33} & r_{34} \\ r_{41} & -r_{42} & r_{43} & r_{44} \end{bmatrix} \begin{bmatrix} C_{mn}^F \\ C_{mn}^w \\ C_{mn}^{f_1} \\ C_{mn}^{f_2} \end{bmatrix} = \begin{bmatrix} 0 \\ 0 \\ 0 \\ 0 \end{bmatrix} \tag{22}$$

where r_{ij} are coefficients and are described in Appendix C.

In order for the system of Eqs. (22) to have a nonzero solution, the determinate of the coefficients is set to zero:

$$\begin{vmatrix} r_{11} & -r_{12} & r_{13} & r_{14} \\ r_{21} & -r_{22} & r_{23} & r_{24} \\ r_{31} & -r_{32} & r_{33} & r_{34} \\ r_{41} & -r_{42} & r_{43} & r_{44} \end{vmatrix} = 0 \tag{23}$$

When the determinant on the left side of the Eq. (23) is expanded, the following expression is obtained for the critical compressive load on the Winkler elastic foundation:

$$N_1 p^2 + N_2 q^2 = \frac{r_{41}K_1 + r_{43}K_3 + r_{44}K_4 + K_2 r_w}{K_2} \tag{24}$$

where

$$K_1 = -\begin{vmatrix} r_{12} & r_{13} & r_{14} \\ r_{22} & r_{23} & r_{24} \\ r_{32} & r_{33} & r_{34} \end{vmatrix}, K_2 = \begin{vmatrix} r_{11} & r_{13} & r_{14} \\ r_{21} & r_{23} & r_{24} \\ r_{31} & r_{33} & r_{34} \end{vmatrix}, K_3 = -\begin{vmatrix} r_{11} & r_{12} & r_{14} \\ r_{21} & r_{22} & r_{24} \\ r_{31} & r_{32} & r_{34} \end{vmatrix}, K_4 = \begin{vmatrix} r_{11} & r_{12} & r_{13} \\ r_{21} & r_{22} & r_{23} \\ r_{31} & r_{32} & r_{33} \end{vmatrix} \tag{25}$$

If $N_2 = \beta N_1 = \beta N$, the dimensional critical biaxial load of nanocomposite rectangular plates on the Winkler elastic foundation in the framework of FSDPT takes the following form:

$$N_{12cr}^{STw} = \frac{r_{41}K_1 + r_{43}K_3 + r_{44}K_4 + K_2 r_w}{K_2(p^2 + \beta q^2)} \tag{26}$$

Here, β is a positive number and ranges from zero to one.

In special cases, if $N_2 = 0$, the rectangular plate will only be subjected to the uniaxial load at x, and the dimensional critical uniaxial load on the Winkler elastic foundation within FSDPT is found from the following expression:

$$N_{1cr}^{STw} = \frac{r_{41}K_1 + r_{43}K_3 + r_{44}K_4 + K_2 r_w}{K_2 p^2} \tag{27}$$

Substituting the first and second terms of expression (21) in the system of Eqs. (19) and applying the Galerkin method, for $N_2 = \beta N_1 = \beta N$, the following expression is obtained for the critical biaxial load on the Winkler elastic foundation within CPT:

$$\bar{N}_{12cr}^{CTw} = \frac{\Gamma + k_1 w}{p^2 + \beta q^2} \tag{28}$$

where

$$\Gamma = \left\{ [d_{13}p^4 + (d_{14} + 2d_{32} + d_{23})p^2q^2 + d_{24}q^4] - [d_{12}p^4 + d_{21}q^4 + (d_{11} - 2d_{31} + d_{22})p^2q^2] \frac{[e_{23}p^4 + (e_{13} - e_{32} + e_{24})p^2q^2 + e_{14}q^4]}{e_{22}p^4 + (e_{12} + e_{31} + e_{21})p^2q^2 + e_{11}q^4} \right\} \tag{29}$$

In special cases, if $N_2 = 0$, the dimensional critical uniaxial load parameter on the Winkler elastic foundation within CPT is found as:

$$N_{1cr}^{CTw} = \frac{\Gamma + k_1 w}{p^2} \tag{30}$$

In the framework of FSDPT and CPT, the following expression is used for the dimensionless values of the uniaxial and critical biaxial load parameters on the Winkler elastic foundation:

$$\bar{N}_{12cr}^{STw} = \frac{N_{12cr}^{STw}}{Y_m h}, \bar{N}_{12cr}^{CTw} = \frac{N_{12cr}^{CTw}}{Y_m h}, \bar{N}_{1cr}^{STw} = \frac{N_{1cr}^{STw}}{Y_m h}, \bar{N}_{1cr}^{CTw} = \frac{N_{1cr}^{CTw}}{Y_m h} \tag{31}$$

5. Results and Discussion

5.1. Comparisons

The accuracy of the proposed method is examined through the buckling analysis example of FG-CNT plates on the Winkler elastic foundation and compared with the magnitudes of critical uniaxial load parameter for the UD, OD and XD-patterns that found by applying the element less-based improved moving least squares-Ritz method in the study of Zhang et al. [29]. In this example, in the framework of FSDPT, the dimensionless critical uniaxial load parameter values of FG-CNT plates on the Winkler elastic foundation for various V_{cnt} are found from the expression $\bar{N}_{1cr}^{STw} = N_{1cr}^{STw} b^2 / E_m h^3$ (See, Table 2). In the comparison with Zhang et al. [29], nanocomposite plates consisting of PmPV and CNTs with the following properties are used: $Y_m = 2.1$ GPa, $V_{cnt} = 0.11$, $\eta_1 = 0.142$, $\eta_2 = \eta_3 = 0.934$, $V_{cnt} = 0.14$, $\eta_1 = 0.15$, $\eta_2 = \eta_3 = 0.941$, $V_{cnt} = 0.17$, $\eta_1 = 0.150$, $\eta_2 = \eta_3 = 1.381$. The Winkler



foundation parameter is expressed as: $K_{1w} = K_w D_m / b^4$. Also, the geometric dimensions of the plate are as follows: $h = 0.002 \text{ m}$, $a / b = 1$, $b = 100h$. Since the wave mode corresponding to the critical load parameter is $(m, n) = (1, 1)$, it is not included in the table. It is seen that the dimensionless critical load values in the presence of the Winkler foundation presented in Table 2 are in agreement with those values presented in Zhang et al. [29].

5.2. Buckling behaviors

In parametric analyses, Polymethyl methacrylate called PMMA, single walled CNTs (SWCNTs) as reinforcing elements are used in the formation of plates, and its properties are given in Table 3 [7].

In the analysis part, the percentages are found from the following expressions: $[N_{12cr}^{CT} - N_{12cr}^{ST}] / N_{12cr}^{CT} \times 100\%$, $[N_{cr}^w - N_{cr}] / N_{cr} \times 100\%$, $[N_{1cr} - N_{12cr}] / N_{12cr} \times 100\%$, $[N_{cr}^{Jg} - N_{cr}^{UD}] / N_{cr}^{UD} \times 100\%$. In the all computations CNT ratio is $V_{cnt}^* = 0.28$. The $K_{1w} = 0$ state corresponds to the groundless state.

The critical values of the uniaxial and biaxial compressive loads depending on the variation of the Winkler soil coefficient are calculated numerically for $T=300\text{K}$, 500K and 700K within the FSDPT and CPT and presented in Table 4. Here $\Gamma_z = 1 - 4z_1^2$ [40-42] is used as the shear deformation shape function and the following data are used: $h=0.002 \text{ m}$, $a / b = 1$, $b / h = 20$, $\beta_0 = 0.5$, $V_{cnt}^* = 28$. As can be seen from Table 4, when the Winkler foundation coefficient increases at room temperature, that is, when $T=300 \text{ K}$, the critical values of both critical uniaxial and biaxial in-plane loads increase, while the wave numbers remain constant. Whereas at $T = 500 \text{ K}$ and 700 K , the critical load values and circumferential wave numbers increase with the increase of K_{1w} . In addition, when T increases, the critical values of uniaxial and biaxial in-plane loads decrease and become less than the critical load values at room temperature, whether with or without foundation. It has been observed that for the critical values of the biaxial load ($\beta_0 = 0.5$), is considerably lower than the critical values of the uniaxial critical load.

In the framework of the FSDPT, when we consider the influences of patterns on the critical load values, it is observed that the effect of patterns on the critical values of the in-plane biaxial load decrease, when K_{1w} and T increases. For instance; at $T = 300 \text{ K}$ the influences on \bar{N}_{12cr}^w for VD, OD and XD-patterns are 20.87%, 35.02% and (-23.57%), respectively; at $T = 500 \text{ K}$ the patterns effects are 19.57%, 33.04% and (-19.79%), respectively, and at $T = 700 \text{ K}$ those effects are 16.73%, 28.75% and (-13.74%), respectively, as $K_{1w} = 400$. The effects of VD, OD and XD-patterns on the $N_{12cr}^w \times 10$, (m, n) for $K_{1w} = 800$ are 18.28%, 30.86% and (-18.56%), and for $K_{1w} = 1200$ those effects are 17.13%, 28.93% and (-17.33%), respectively, at $T = 500 \text{ K}$.

As for the influence of shear deformations (SDs), considering the ground effect significantly reduces the SDs effect on the in-plane critical loads. The SDs effect on the critical value of the biaxial load is significantly reduced compared to the critical uniaxial load. Since the temperature increase especially affects the SDs effect more, it threatens the stability of the plates. It turns out that the SDs effect is lower in critical biaxial loads compared to critical uniaxial loads. In presence of ground, the maximum SDs effects on the critical uniaxial and biaxial load are 55.63% and 41.29%, respectively, for XD-pattern at $K_{1w} = 400$ and $T = 700 \text{ K}$, while the least influences of SDs effects on the \bar{N}_{1cr}^w and \bar{N}_{12cr}^w are 11.5% and 9.63%, respectively, when $K_{1w} = 1200$ and $T = 300 \text{ K}$ for the OD-pattern. When UD, VD, OD and XD patterns are compared among themselves, the most obvious ground effect on critical uniaxial and biaxial loads occurs in the OD-patterned with 41.27%, and 28.02% at $T = 700 \text{ K}$ and $K_{1w} = 1200$ (see, Table 4).

Table 2. Comparison of the critical load parameter values of FG-CNT plates on the Winkler elastic foundation with the results of Zhang et al. [29] for different V_{cnt}^* and CNT patterns.

Pattern types	CNT ratio (%) V_{cnt}^*	\bar{N}_{1cr}^{STw}			
		$K_{1w} = 10^2$		$K_{1w} = 10^3$	
		Zhang et al. [29]	Present study FSDPT	Zhang et al. [29]	Present study FSDPT
UD	11	40.066	40.294	48.609	48.887
	14	50.028	50.336	58.501	58.929
	17	58.421	61.407	66.908	66.584
OD	11	22.280	22.429	30.809	31.022
	14	27.308	27.520	35.858	36.112
	17	32.167	33.678	40.715	42.270
XD	11	57.687	57.992	66.228	66.585
	14	72.501	72.872	81.041	81.464
	17	84.564	88.935	93.109	97.527

Table 3. Properties of matrix and reinforced components.

Properties of PMMA	Properties of CNTs	The efficiency parameters of CNTs
$Y_m = 2.5 \times 10^9 \text{ Pa}$, $\nu_m = 0.34$ $\rho_m = 1150 \text{ kg/m}^3$	$Y_{11}^{cnt} = 5.6466 \text{ TPa}$, $Y_{22}^{cnt} = 7.08 \text{ TPa}$, $Y_{12}^{cnt} = 1.9445 \text{ TPa}$, $\nu_{12}^{cnt} = 0.175$, $\rho_{cnt} = 1400 \text{ kg/m}^3$	$\eta_1 = 0.137$, $\eta_2 = 1.022$, $\eta_3 = 0.715$ at $V_{cnt}^* = 0.12$ $\eta_1 = 0.142$, $\eta_2 = 1.626$, $\eta_3 = 1.138$ at $V_{cnt}^* = 0.17$ $\eta_1 = 0.141$, $\eta_2 = 1.585$, $\eta_3 = 1.109$ at $V_{cnt}^* = 0.28$
	Geometrical properties of SWCNTs	
$\bar{r} = 9.26 \text{ nm}$, $\bar{a} = 0.68 \text{ nm}$, $\bar{h} = 0.067 \text{ nm}$		



Table 4. Variation of the critical values of the x-direction and biaxial compressive loads in the framework of FSDPT and CPT for different T depending on the variation of the Winkler soil coefficient

$\bar{N}_{1cr}^w \times 10, (m, n), T = 300 \text{ K}$								
	FSDPT	CPT	FSDPT	CPT	FSDPT	CPT	FSDPT	CPT
K_{1w}	UD		VD		OD		XD	
0	1.424(1,1)	1.971(1,1)	1.107(1,1)	1.378(1,1)	0.891(1,1)	1.044(1,1)	1.782(1,1)	2.911(1,1)
400	1.519(1,1)	2.066(1,1)	1.202(1,1)	1.474(1,1)	0.987(1,1)	1.140(1,1)	1.877(1,1)	3.007(1,1)
800	1.615(1,1)	2.162(1,1)	1.298(1,1)	1.569(1,1)	1.082(1,1)	1.235(1,1)	1.973(1,1)	3.102(1,1)
1200	1.710(1,1)	2.257(1,1)	1.393(1,1)	1.664(1,1)	1.178(1,1)	1.331(1,1)	2.068(1,1)	3.198(1,1)
$\bar{N}_{12cr}^w \times 10, (m, n), T = 300 \text{ K}$								
0	0.744(1,2)	0.958(1,2)	0.660(1,2)	0.779(1,2)	0.542(1,2)	0.610(1,2)	0.921(1,2)	1.349(1,2)
400	0.776(1,2)	0.989(1,2)	0.692(1,2)	0.811(1,2)	0.574(1,2)	0.642(1,2)	0.953(1,2)	1.381(1,2)
800	0.808(1,2)	1.021(1,2)	0.724(1,2)	0.843(1,2)	0.606(1,2)	0.674(1,2)	0.985(1,2)	1.413(1,2)
1200	0.840(1,2)	1.053(1,2)	0.756(1,2)	0.875(1,2)	0.638(1,2)	0.706(1,2)	1.017(1,2)	1.445(1,2)
$\bar{N}_{1cr}^w \times 10, (m, n), T = 500 \text{ K}$								
0	1.248(1,1)	1.895(1,1)	0.985(1,1)	1.310(1,1)	0.804(1,1)	0.990(1,1)	1.515(1,1)	2.810(1,1)
400	1.344(1,1)	1.991(1,1)	1.081(1,1)	1.405(1,1)	0.900(1,1)	1.086(1,1)	1.610(1,1)	2.905(1,1)
800	1.439(1,1)	2.086(1,1)	1.176(1,1)	1.501(1,1)	0.995(1,1)	1.181(1,1)	1.706(1,1)	3.001(1,1)
1200	1.535(1,1)	2.181(1,1)	1.272(1,1)	1.596(1,1)	1.091(1,1)	1.277(1,1)	1.801(1,1)	3.096(1,1)
$\bar{N}_{12cr}^w \times 10, (m, n), T = 500 \text{ K}$								
0	0.610(1,2)	0.850(1,2)	0.537(1,2)	0.669(1,2)	0.445(1,2)	0.521(1,2)	0.740(1,2)	1.212(1,2)
400	0.641(1,2)	0.882(1,2)	0.569(1,2)	0.701(1,2)	0.476(1,2)	0.552(1,2)	0.771(1,2)	1.236(1,3)
800	0.673(1,2)	0.914(1,2)	0.601(1,2)	0.733(1,2)	0.508(1,2)	0.584(1,2)	0.803(1,2)	1.254(1,3)
1200	0.705(1,2)	0.946(1,2)	0.633(1,2)	0.765(1,2)	0.540(1,2)	0.616(1,2)	0.835(1,2)	1.271(1,3)
$\bar{N}_{1cr}^w \times 10, (m, n), T = 700 \text{ K}$								
0	1.010 (1,1)	1.840 (1,1)	0.825 (1,1)	1.256 (1,1)	0.693 (1,1)	0.946 (1,1)	1.163 (1,1)	2.740 (1,1)
400	1.106 (1,1)	1.935 (1,1)	0.921 (1,1)	1.351 (1,1)	0.788 (1,1)	1.042 (1,1)	1.258 (1,1)	2.835 (1,1)
800	1.201 (1,1)	2.031 (1,1)	1.016 (1,1)	1.447 (1,1)	0.884 (1,1)	1.137 (1,1)	1.354 (1,1)	2.931 (1,1)
1200	1.297 (1,1)	2.126 (1,1)	1.112 (1,1)	1.542 (1,1)	0.979 (1,1)	1.233 (1,1)	1.449 (1,1)	3.026 (1,1)
$\bar{N}_{12cr}^w \times 10, (m, n), T = 700 \text{ K}$								
0	0.455 (1,2)	0.684 (1,3)	0.402 (1,2)	0.563 (1,2)	0.339 (1,2)	0.434 (1,2)	0.531 (1,2)	0.941 (1,3)
400	0.486 (1,2)	0.701 (1,3)	0.434 (1,2)	0.595 (1,2)	0.370 (1,2)	0.466 (1,2)	0.563 (1,2)	0.959 (1,3)
800	0.518 (1,2)	0.718 (1,3)	0.466 (1,2)	0.627 (1,2)	0.402 (1,2)	0.498 (1,2)	0.594 (1,2)	0.976 (1,3)
1200	0.540 (1,3)	0.736 (1,3)	0.498 (1,2)	0.649 (1,3)	0.434 (1,2)	0.526 (1,3)	0.626 (1,2)	0.993 (1,3)

The variation of the critical values of biaxial compressive load of nanocomposite plates with and without Winkler elastic foundation within FSDPT and CPT for different T versus the b/h are given in Table 5. The following data are used $h=0.002 \text{ m}, a/b=1, \beta_0=0.5, V_{crit}=28$. As can be seen from Table 5, when the b/h ratio increases from 20 to 50, the values of the critical biaxial load increase, while the number of waves in the x direction equals one and is independent of the b/h ratio. It was observed that while the number of waves in the y direction remained constant within the determined range of the b/h ratio, it increased depending on the increase in T .

In the framework of FSDPT, when the effect of patterns on the critical biaxial load of the plate is investigated, it is seen that the effects of UD, VD, OD and XD-patterns on the critical biaxial load increase when the b/h ratio increases, and also the presence of Winkler elastic foundation weakens those effects relatively. For instance; at $T=300 \text{ K}$ and for $K_{1w}=0$; when the b/h ratio increases from 20 to 50, the influences of UD, VD, OD and XD-patterns on \bar{N}_{12cr} increment from 11.29% to 17.12%, from 27.15% to 34.25% and from (-23.79%) to (-36.33%), respectively, those effects on the \bar{N}_{12cr}^w increase from 10.19% to 15.72%, from 24.52% to 32.08%, and from (-21.48%) to (-37.01%), respectively, for $K_{1w}=1000$. When the temperature T increases, the effect of the patterns on the critical biaxial load differs. The influences of the patterns on the critical biaxial load are pronounced for $T=500 \text{ K}$ compared to $T=300 \text{ K}$, while those effects are weakened for $T=700 \text{ K}$ compared to $T=500 \text{ K}$.

When the effects of the transverse shear deformations on the critical values of biaxial load are investigated, it is observed that the SDs effects decrease significantly with the increase of the b/h ratio from 20 to 50 in the grounded and unground conditions, and the difference between FSDPT and CPT can be negligible in the subsequent increases of b/h . In addition, it was concluded that the increase of T weakens the decrease of the effect of SDs on the value of the critical biaxial load, but the presence of K_{1w} weakens the effect of SDs. For example, At $b/h=20$ and for $K_{1w}=0$, the effects of SDs on the critical value of biaxial load of the VD-patterned plate are 15.28%, 19.73% and 28.6% for $T=300 \text{ K}, 500 \text{ K}$ and 700 K , respectively, while these effects are 13.85%, 17.62% and 24.69%, respectively, for $K_{1w}=1000$. At $b/h=50$, the effects of SDs on the critical values of the biaxial load of the VD-patterned plate for $T=300 \text{ K}, 500 \text{ K}$ and 700 K are 3.2%, 3.74% and 6.67%, respectively, when $K_{1w}=0$, while those influences are 2.19%, 14.17% and 4.9%, respectively, for $K_{1w}=1000$.



Table 5. Variation of the critical values of biaxial compressive load of nanocomposite plates with and without Winkler elastic foundation within FSDPT and CPT for different T versus b/h

		$\bar{N}_{12cr}^w \times 10, (m, n)$							
		UD		VD		OD		XD	
		FSDPT	CPT	FSDPT	CPT	FSDPT	CPT	FSDPT	CPT
b/h		$T = 300 \text{ K}, K_{1w} = 0$							
20		0.744(1,2)	0.958(1,2)	0.660(1,2)	0.779(1,2)	0.542(1,2)	0.610(1,2)	0.921(1,2)	1.349(1,2)
30		0.376(1,2)	0.426(1,2)	0.320(1,2)	0.346(1,2)	0.257(1,2)	0.271(1,2)	0.492(1,2)	0.600(1,2)
40		0.222(1,2)	0.239(1,2)	0.186(1,2)	0.195(1,2)	0.148(1,2)	0.153(1,2)	0.299(1,2)	0.337(1,2)
50		0.146(1,2)	0.153(1,2)	0.121(1,2)	0.125(1,2)	0.096(1,2)	0.098(1,2)	0.199(1,2)	0.216(1,2)
b/h		$T = 300 \text{ K}, K_{1w} = 1000$							
20		0.824(1,2)	1.037(1,2)	0.740(1,2)	0.859(1,2)	0.622(1,2)	0.690(1,2)	1.001(1,2)	1.429(1,2)
30		0.411(1,2)	0.461(1,2)	0.355(1,2)	0.382(1,2)	0.292(1,2)	0.307(1,2)	0.527(1,2)	0.635(1,2)
40		0.242(1,2)	0.259(1,2)	0.206(1,2)	0.215(1,2)	0.168(1,2)	0.172(1,2)	0.319(1,2)	0.357(1,2)
50		0.159(1,2)	0.166(1,2)	0.134(1,2)	0.137(1,2)	0.108(1,2)	0.110(1,2)	0.212(1,2)	0.229(1,2)
b/h		$T = 500 \text{ K}, K_{1w} = 0$							
20		0.610(1,2)	0.850(1,2)	0.537(1,2)	0.669(1,2)	0.445(1,2)	0.521(1,2)	0.740(1,2)	1.212(1,2)
30		0.319(1,2)	0.378(1,2)	0.267(1,2)	0.297(1,2)	0.215(1,2)	0.231(1,2)	0.413(1,2)	0.539(1,2)
40		0.192(1,2)	0.213(1,2)	0.157(1,2)	0.167(1,2)	0.125(1,2)	0.130(1,2)	0.258(1,2)	0.303(1,2)
50		0.127(1,2)	0.136(1,2)	0.103(1,2)	0.107(1,2)	0.081(1,2)	0.083(1,2)	0.174(1,2)	0.194(1,2)
b/h		$T = 500 \text{ K}, K_{1w} = 1000$							
20		0.689(1,2)	0.930(1,2)	0.617(1,2)	0.749(1,2)	0.524(1,2)	0.600(1,2)	0.819(1,2)	1.263(1,3)
30		0.354(1,2)	0.413(1,2)	0.302(1,2)	0.333(1,2)	0.250(1,2)	0.267(1,2)	0.448(1,2)	0.561(1,3)
40		0.212(1,2)	0.232(1,2)	0.177(1,2)	0.187(1,2)	0.144(1,2)	0.150(1,2)	0.278(1,2)	0.316(1,3)
50		0.140(1,2)	0.149(1,2)	0.115(1,2)	0.120(1,2)	0.094(1,2)	0.096(1,2)	0.187(1,2)	0.202(1,3)
b/h		$T = 700 \text{ K}, K_{1w} = 0$							
20		0.455 (1,2)	0.684 (1,3)	0.402 (1,2)	0.563 (1,2)	0.339 (1,2)	0.434 (1,2)	0.531 (1,2)	0.941 (1,3)
30		0.253 (1,3)	0.304 (1,3)	0.211 (1,2)	0.250 (1,2)	0.170 (1,2)	0.193 (1,2)	0.316 (1,3)	0.418 (1,3)
40		0.152 (1,3)	0.171 (1,3)	0.127 (1,2)	0.140 (1,2)	0.101 (1,2)	0.108 (1,2)	0.197 (1,3)	0.235 (1,3)
50		0.101 (1,3)	0.109 (1,3)	0.084 (1,2)	0.090 (1,2)	0.066 (1,2)	0.069 (1,2)	0.133 (1,3)	0.150 (1,3)
b/h		$T = 700 \text{ K}, K_{1w} = 1000$							
20		0.532 (1,3)	0.727 (1,3)	0.482 (1,2)	0.640 (1,3)	0.418 (1,2)	0.514 (1,2)	0.610 (1,2)	0.985 (1,3)
30		0.272 (1,3)	0.323 (1,3)	0.246 (1,2)	0.284 (1,3)	0.206 (1,2)	0.228 (1,2)	0.335 (1,3)	0.437 (1,3)
40		0.163 (1,3)	0.181 (1,3)	0.147 (1,2)	0.160 (1,3)	0.121 (1,2)	0.128 (1,2)	0.207 (1,3)	0.246 (1,3)
50		0.108 (1,3)	0.116 (1,3)	0.097 (1,2)	0.102 (1,3)	0.079 (1,2)	0.082 (1,2)	0.140 (1,3)	0.157 (1,3)

The variations of the critical values of biaxial compressive load of nanocomposite plates with and without Winkler elastic foundation within FSDPT and CPT for different T versus the β_0 are illustrated in Figs. 3-6. The following data are used: $h=0.002 \text{ m}$, $a/b=1$, $b/h=20$, $V_{crit}^* = 28$. In this table, $\beta_0 = 0$ corresponds to uniaxial loading. It is observed that the critical values of biaxial load presented in Table 6 are smaller than the critical values of uniaxial load, and this decrease becomes more evident when β_0 increases from 0.2 to 1.0. When the effect of the patterns on the critical biaxial load is investigated in the change of β_0 , the following results emerge. Although the effect of patterns on the critical biaxial load is close to the critical biaxial load at β_0 close to zero (for example, $\beta_0 \leq 0.2$), there is a weak decrease in the VD and OD-patterns, whereas there is a weak increase in the XD-pattern. The subsequent increase of β_0 reveals an irregularity and difference in pattern effects. For example, with and without Winkler foundation cases, at $T = 300 \text{ K}$ and 500 K , and without foundation for $T = 700 \text{ K}$ also (see, Figs. 3 and 4); in the range $\beta_0 \in [0.2, 1.0]$, the effects of VD, OD and XD-patterns on the critical biaxial load change parabolic, that is, it first decreases and then increases after taking the minimum value. At $T = 700 \text{ K}$, while the VD and OD-patterns effects on the critical value of the biaxial load in the grounded condition ($K_{1w} = 1000$) are continuously reduced, the XD-pattern effect is continuously increased (see, Figs. 4 and 5).

For $T = 300 \text{ K}$ and 500 K , with and without ground conditions, when β_0 increases from 0.2 to 1.0, the effect of SDs on the critical biaxial load first reduces, reaches a minimum, and then increases in UD, VD, OD and XD-patterns. Considering the $T = 700 \text{ K}$ and grounded condition, the effect of SDs on the critical biaxial load shows a continuous reduction in VD, OD and XD-patterned plates. The most obvious SDs effect on the critical biaxial load is 51.11% in ungrounded plate and 47.2% in the plate on the ground for $\beta_0 = 0.2$, while those effects are 38.49% in unconstrained plate and 36.41% in grounded condition for $\beta_0 = 1.0$. It is observed that the prominence of the influence of SDs on the critical biaxial load decreases, respectively, in UD, VD and XD-patterns. In cases of $T = 300 \text{ K}$ and 500 K , the ground effect can make the effect of the UD-pattern on the critical biaxial load independent of β_0 , whereas for XD-pattern this only occurs at $T = 300 \text{ K}$.



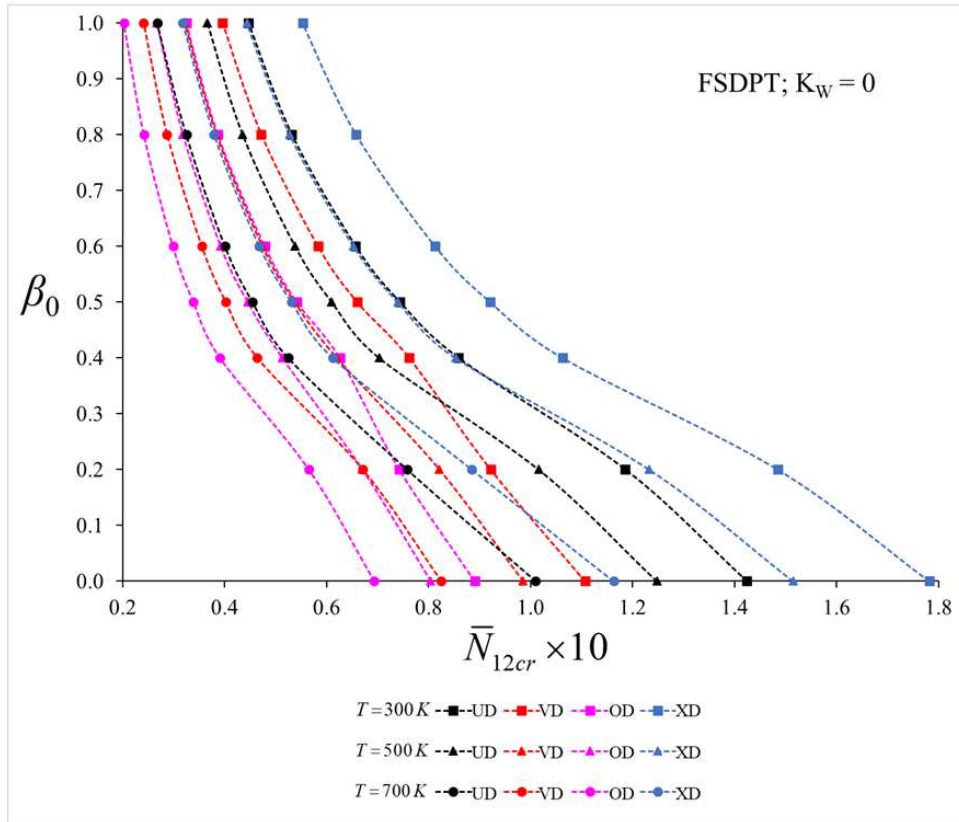


Fig. 3. Variation of the critical values of biaxial compressive load of unconstrained nanocomposite plates within FSDPT for different T versus β_0 .

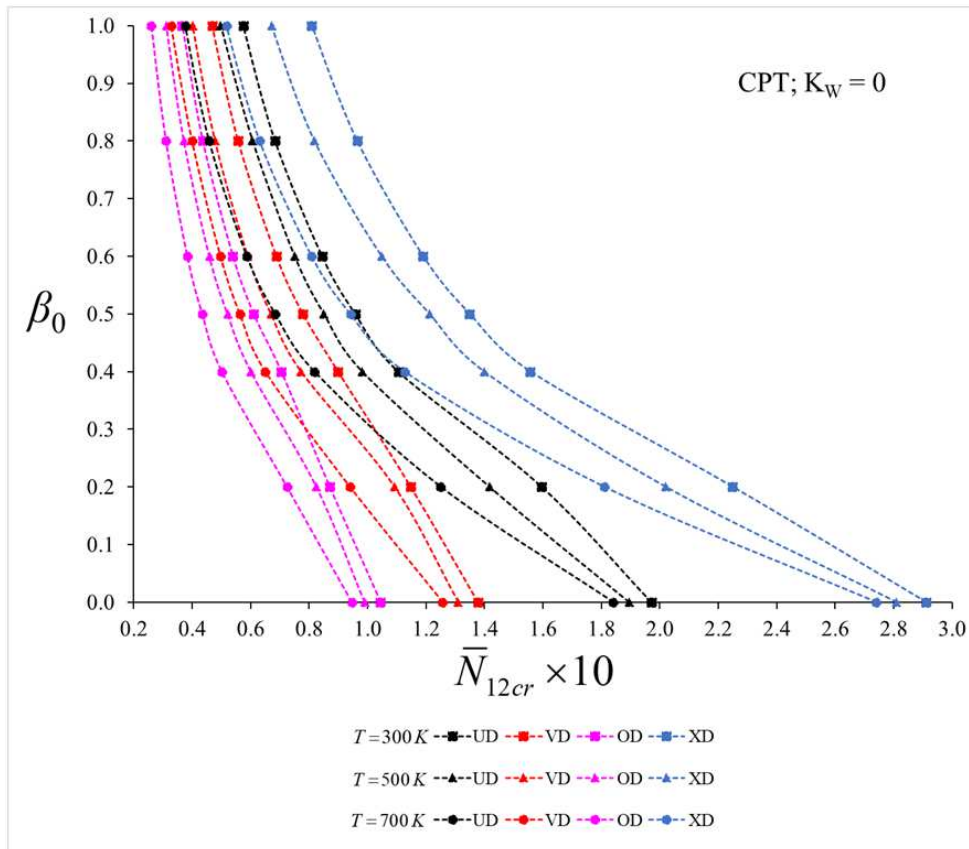


Fig. 4. Variation of the critical values of biaxial compressive load of unconstrained nanocomposite plates within CPT for different T versus β_0 .



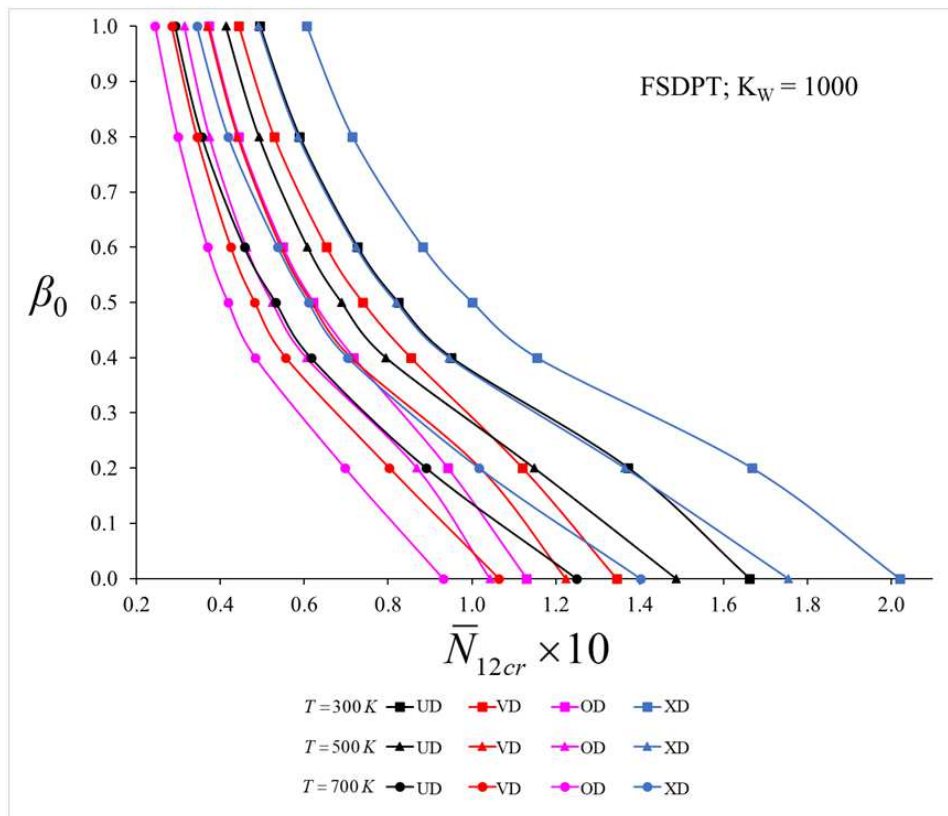


Fig. 5. Variation of the critical values of biaxial compressive load of nanocomposite plates on Winkler elastic foundation within FSDPT for different T versus β_0 .

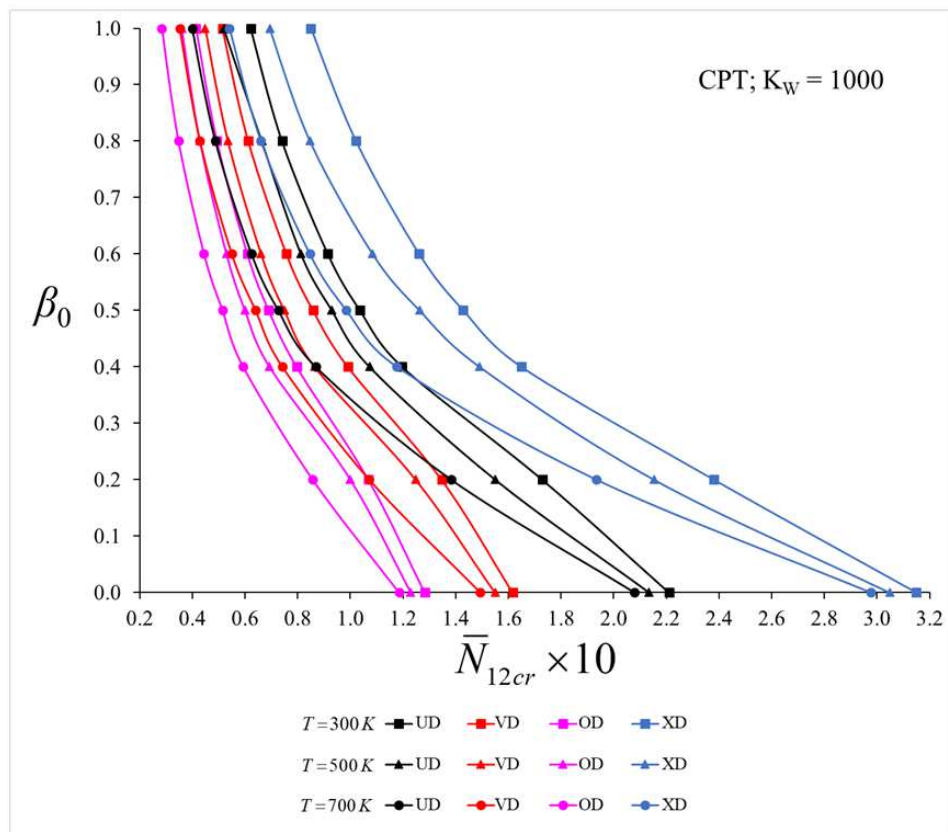


Fig. 6. Variation of the critical values of biaxial compressive load of nanocomposite plates on Winkler elastic foundation within CPT for different T versus β_0 .



6. Conclusions

The buckling behavior of moderately-thick nanocomposite plates under in-plane compressive loads on Winkler elastic foundation and thermal environments in the framework of FSDPT and CPT was investigated. First, the temperature-dependent properties of CNTs and nanocomposites were defined and their constitutive relations were established, then the stability and strain compatibility equations on Winkler elastic foundation were derived in the framework of the FSDPT and CPT. Then, applying the Galerkin method to the basic equations, the closed-form solution was obtained for the critical uniaxial and biaxial compressive loads. The specific numerical analyzes and interpretations were made for various plate sizes, volume fraction fractions and CNT patterns in elastic and thermal environments within FSDPT and CPT.

Author Contributions

Conceptualization, A.H. Sofiyev and N. Fantuzzi; methodology, A.H. Sofiyev, N. Fantuzzi and C. Ipek; software, C. Ipek and S.P. Efendiyeva; validation, C. Ipek and A.H. Sofiyev; investigation, C. Ipek; resources, C. Ipek and S.P. Efendiyeva; writing—original draft preparation, C. Ipek and A.H. Sofiyev; writing—review and editing, N. Fantuzzi, A.H. Sofiyev, C. Ipek and S.P. Efendiyeva.

Acknowledgments

Not Applicable

Conflict of Interest

The authors declared no potential conflicts of interest with respect to the research, authorship and publication of this article.

Funding

The authors received no financial support for the research, authorship and publication of this article

Data Availability Statements

The datasets generated and/or analyzed during the current study are available from the corresponding author on reasonable request.

References

- [1] Lee, D.J., Kumar, V., Rubber Nanocomposites Reinforced with Single-Wall and Multiwall Carbon Nanotubes for Industrial Applications, *Rubber Chemistry and Technology*, 93(1), 2020, 157–171.
- [2] Dresselhaus, M.S., Dresselhaus, G., Charlier, J.C., Hernandez, E., Electronic, Thermal and Mechanical Properties of Carbon Nanotubes, *Philosophical transactions. Series A, Mathematical, Physical, and Engineering Sciences*, 362(1823), 2004, 2065–2098.
- [3] Rahman, G., Najaf, Z., Mehmood, A., Bilal, S., Shah, A., Mian, S., Ali, G., An Overview of the Recent Progress in the Synthesis and Applications of Carbon Nanotubes, *Journal of Carbon Research*, 5(1), 2019, 1–31.
- [4] Kumanek, B., Janas, D., Thermal conductivity of carbon nanotube networks: a review, *Journal of Materials Science*, 54(10), 2019, 7397–7427.
- [5] Ma, P.C., Siddiqui, N.A., Marom, G., Kim, J.K., Dispersion and Functionalization of Carbon Nanotubes for Polymer-Based Nanocomposites: A Review, *Composites Part A: Applied Science and Manufacturing*, 41(10), 2010, 1345–1367.
- [6] Khan, W., Sharma, R., Saini, P., *Carbon Nanotube-Based Polymer Composites: Synthesis, Properties and Applications*, Intech Open, 2016.
- [7] Shen, H.S., Nonlinear Bending Of Functionally Graded Carbon Nanotube Reinforced Composite Plates In Thermal Environments, *Composite Structures*, 91(1), 2009, 9–19.
- [8] Lei, Z.X., Liew, K.M., Yu, J.L., Buckling Analysis of Functionally Graded Carbon Nanotube-Reinforced Composite Plates Using the Element-Free Kp-Ritz Method, *Composite Structures*, 98, 2013, 160–168.
- [9] Lei, Z.X., Zhang, L.W., Liew, K.M., Buckling Analysis of CNT Reinforced Functionally Graded Laminated Composite Plates, *Composite Structures*, 152, 2016, 62–73.
- [10] Mirzaei, M., Kiani, Y., Thermal Buckling of Temperature Dependent FG-CNT Reinforced Composite Plates, *Meccanica*, 51(9), 2016, 2185–2201.
- [11] Kiani, Y., Shear buckling of FG-CNT Reinforced Composite Plates using Chebyshev-Ritz method, *Composites Part B: Engineering*, 105, 2016, 176–187.
- [12] Kiani, Y., Buckling of FG-CNT-Reinforced Composite Plates Subjected to Parabolic Loading, *Acta Mechanica*, 228(4), 2017, 1303–1319.
- [13] George, N., Jeyaraj, P., Murigendrappa, S.M., Buckling and Free Vibration of Nonuniformly Heated Functionally Graded Carbon Nanotube Reinforced Polymer Composite Plate, *International Journal of Structural Stability and Dynamics*, 17(6), 2017, 1750064.
- [14] Farzam, A., Hassani, B., Thermal and Mechanical Buckling Analysis of FG Carbon Nanotube Reinforced Composite Plates Using Modified Couple Stress Theory and Isogeometric Approach, *Composite Structures*, 206, 2018, 774–790.
- [15] Jiao, P., Chen, Z., Ma, H., Zhang, D., Ge, P., Buckling Analysis of Thin Rectangular FG-CNTRC Plate Subjected to Arbitrarily Distributed Partial Edge Compression Loads Based on Differential Quadrature Method, *Thin-Walled Structures*, 145, 2019, 106417.
- [16] Sedighi, H.M., Divergence and Flutter Instability of Magneto-Thermo-Elastic C-BN Hetero-Nanotubes Conveying Fluid, *Acta Mechanica Sinica*, 36, 2020, 381–396.
- [17] Abouelregal, A.E., Mohammad-Sedighi, H., Faghidian, S.A., Shirazi, A.H., Temperature-Dependent Physical Characteristics of the Rotating Nonlocal Nanobeams Subject to a Varying Heat Source and a Dynamic Load, *Facta Universitatis, Series: Mechanical Engineering*, 19(4), 2021, 633–656.
- [18] Bhagat, V.S., George, N., Arunkumar, M.P., Pitchaimani, J., Lenin Babu, M.C., Numerical Analysis on Vibro-Acoustic Behavior of Honeycomb Core Sandwich Structure with FG-CNT-Reinforced Polymer Composite Facings, *Iranian Journal of Science and Technology, Transactions of Mechanical Engineering*, 46, 2022, 943–956.
- [19] Van Tien, N., Phuong, N.T., Duc, V.M., Minh, T.Q., Dong, D.T., Quan, P.H., Nam, V.H., Ly, L.N., Nonlinear Thermo-Mechanical Buckling of Torsion-Loaded Cylindrical Shells with Eccentric Stiffeners Made from CNT-Reinforced Composite, *Iranian Journal of Science and Technology, Transactions of Mechanical Engineering*, 46, 2022, 1107–1119.
- [20] Bachiri, A., Daikh, A.A., Tounsi, A., On the Thermo-elastic Response of FG-CNTRC Cross-ply Laminated Plates under Temperature Loading using a New HSDT, *Journal of Applied and Computational Mechanics*, 8(4), 2022, 1370–1386.
- [21] Malekzadeh Fard, K., Khajehdehi Kavanroodi, M., Malek-Mohammadi, H., Pourmoayed, A., Buckling and Vibration Analysis of a Double-layer Graphene Sheet Coupled with a Piezoelectric Nanoplate, *Journal of Applied and Computational Mechanics*, 8(1), 2022, 129–143.
- [22] Baccocchi, M., Fantuzzi, N., Luciano, R., Tarantino, A.M., Finite Element Solution of Vibrations and Buckling of Laminated Thin Plates in Hygro-Thermal Environment Based on Strain Gradient Theory, *Mechanics Based Design of Structures and Machines*, 2022, 1–14. DOI: 10.1080/15376494.2022.2093425.
- [23] Saitta, S., Luciano, R., Vescovini, R., Fantuzzi, N., Fabbrocino, F., Free Vibrations and Buckling Analysis of Cross-Ply Composite Nanoplates by Means of a Mesh Free Radial Point Interpolation Method, *Composite Structures*, 298, 2022, 115989.



- [24] Tornabene, F., Fantuzzi, N., Baccocchi, M., Linear static response of nanocomposite plates and shells reinforced by agglomerated carbon nanotubes, *International Workshop Multi-Scale Innovations of Material Structures (MIMS)*, 115, 2017, 449-476.
- [25] Sofiyev, A., Usame, K., Investigation of Buckling Behavior of Functionally Graded Carbon Nanotube Patterned Polymer Plates in Thermal Environments, *UNEC Journal of Engineering and Applied Sciences*, 2(1), 2022, 19-25.
- [26] Hu, Z., Zhou, C., Ni, Z., Lin, X., Li, R., New Symplectic Analytic Solutions for Buckling of CNT Reinforced Composite Rectangular Plates, *Composite Structures*, 303, 2023, 116361.
- [27] Babaei, H., Thermoelastic Buckling and Post-Buckling Behavior of Temperature-Dependent Nanocomposite Pipes Reinforced with CNTs, *European Physical Journal Plus*, 136(10), 2021. DOI: 10.1140/epjp/s13360-021-01992-x.
- [28] Babaei, H., Kiani, Y., Eslami, M.R., Perturbation Method for Thermal Post-Buckling Analysis of Shear Deformable FG-CNTRC Beams with Different Boundary Conditions, *International Journal of Structural Stability and Dynamics*, 21(13), 2021, 2150175.
- [29] Zhang, L.W., Lei, Z.X., Liew, K.M., An Element-free IMLS-Ritz Framework for Buckling Analysis of FG-CNT Reinforced Composite Thick Plates Resting on Winkler Foundations, *Engineering Analysis with Boundary Elements*, 58, 2015, 7-17.
- [30] Tung, H.V., Thermal and Thermomechanical Postbuckling of FGM Sandwich Plates Resting on Elastic Foundations with Tangential Edge Constraints and Temperature Dependent Properties, *Composite Structures*, 131, 2015, 1028-1039.
- [31] Wattanasakulpong, N., Chaikittiratanana, A., Exact Solutions for Static and Dynamic Analyses of Carbon Nanotube-Reinforced Composite Plates with Pasternak Elastic Foundation, *Applied Mathematical Modeling*, 39(18), 2015, 5459-5472.
- [32] Lei, Z.X., Zhang, L.W., Liew, K.M., Buckling of FG-CNT Reinforced Composite Thick Skew Plates Resting on Pasternak Foundations Based on an Element-Free Approach, *Applied Mathematics and Computation*, 266, 2015, 773-791.
- [33] Zhang, L.W., Liew, K.M., Postbuckling Analysis of Axially Compressed CNT Reinforced Functionally Graded Composite Plates Resting on Pasternak Foundations Using an Element-Free Approach, *Composite Structures*, 138, 2016, 40-51.
- [34] Tung, H.V., Thermal Buckling and Postbuckling Behavior of Functionally Graded Carbon Nanotube-Reinforced Composite Plates Resting on Elastic Foundations with Tangential-Edge Restraints, *Journal of Thermal Stresses*, 40(5), 2017, 641-663.
- [35] Zhong, R., Wang, Q., Tang, J., Shuai, C., Liang, Q., Vibration Characteristics of Functionally Graded Carbon Nanotube Reinforced Composite Rectangular Plates on Pasternak Foundation with Arbitrary Boundary Conditions and Internal Line Supports, *Curved and Layered Structures*, 5, 2018, 10-34.
- [36] Long, V.T., Tung, H.V., Thermomechanical Postbuckling Behavior of CNT-Reinforced Composite Sandwich Plate Models Resting on Elastic Foundations with Elastically Restrained Unloaded Edges, *Journal of Thermal Stresses*, 42(5), 2019, 658-680.
- [37] Babaei, H., Thermomechanical Analysis of Snap-Buckling Phenomenon in long FG-CNTRC Cylindrical Panels Resting on Nonlinear Elastic Foundation, *Composite Structures*, 286, 2022, 115199.
- [38] Hieu, D.V., Phi, B.G., Sedighi, H.M., Sofiyev, A.H., Size-Dependent Nonlinear Vibration of Functionally Graded Composite Micro-Beams Reinforced by Carbon Nanotubes with Piezoelectric Layers in Thermal Environments, *Acta Mechanica*, 233, 2022, 2249-2270.
- [39] Sofiyev, A.H., Kadioglu, F., Khalilov, I.A., Sedighi, H.M., Vergul, T., Yenialp, R., On the Torsional Buckling Moment of Cylindrical Shells Consisting of Functionally Graded Materials Resting on the Pasternak-Type Soil, *SOCAR Proceedings*, S11, 2022, 016-022.
- [40] Ambartsumyan, S.A., *Theory of Anisotropic Plates*, Nauka, Moscow, 1967 [in Russian]
- [41] Eslami, M.R., *Buckling and Postbuckling of Beams, Plates and Shells*, Springer, Switzerland, 2018.
- [42] Amabili, M., *Nonlinear Vibrations and Stability of Shells and Plates*, Cambridge University Press, New York, 2008.
- [43] Akhmedov, N.K., Mektiyev, M.F., The Axisymmetric Problem of the Theory of Elasticity for a Non-Uniform Plate of Variable Thickness, *Journal of Applied Mathematics and Mechanics*, 59(3), 1995, 491-495.

Appendix A

L_{ij} are differential operators and defined as:

$$\begin{aligned}
 L_{11} &= h(d_{11} - d_{31}) \frac{\partial^4}{\partial x^2 \partial y^2} + h d_{12} \frac{\partial^4}{\partial x^4}, \quad L_{12} = -d_{13} \frac{\partial^4}{\partial x^4} - (d_{14} + d_{32}) \frac{\partial^4}{\partial x^2 \partial y^2} \\
 L_{13} &= d_{15} \frac{\partial^3}{\partial x^3} + d_{35} \frac{\partial^3}{\partial x \partial y^2} - \delta_3 \frac{\partial}{\partial x}, \quad L_{14} = d_{18} \frac{\partial^3}{\partial x^2 \partial y} + d_{38} \frac{\partial^3}{\partial x^2 \partial y}, \\
 L_{21} &= h d_{21} \frac{\partial^4}{\partial y^4} + h(d_{22} - d_{31}) \frac{\partial^4}{\partial x^2 \partial y^2}, \quad L_{22} = -(d_{32} + d_{23}) \frac{\partial^4}{\partial x^2 \partial y^2} - d_{24} \frac{\partial^4}{\partial y^4}, \\
 L_{23} &= (d_{25} + d_{35}) \frac{\partial^3}{\partial x \partial y^2}, \quad L_{24} = d_{38} \frac{\partial^3}{\partial x^2 \partial y} + d_{28} \frac{\partial^3}{\partial y^3} - \delta_4 \frac{\partial}{\partial y} \\
 L_{31} &= e_{11} \frac{\partial^4}{\partial y^4} + (e_{12} + e_{21} + e_{31}) \frac{\partial^4}{\partial x^2 \partial y^2} + e_{22} \frac{\partial^4}{\partial x^4}, \quad L_{32} = -e_{23} \frac{\partial^4}{\partial x^4} - (e_{24} + e_{13} - e_{32}) \frac{\partial^4}{\partial x^2 \partial y^2} - e_{14} \frac{\partial^4}{\partial y^4} \\
 L_{33} &= e_{15} \frac{\partial^3}{\partial x \partial y^2} + e_{25} \frac{\partial^3}{\partial x^3} + e_{35} \frac{\partial^3}{\partial x \partial y^2}, \quad L_{34} = e_{18} \frac{\partial^3}{\partial y^3} + e_{28} \frac{\partial^3}{\partial x^2 \partial y} + e_{38} \frac{\partial^3}{\partial x^2 \partial y} \\
 L_{41} &= 0, \quad L_{42} w = -N_1 \frac{\partial^2}{\partial x^2} - N_2 \frac{\partial^2}{\partial y^2} + k_1, \quad L_{43} = \delta_3 \frac{\partial}{\partial x}, \quad L_{44} = \delta_4 \frac{\partial}{\partial y}
 \end{aligned} \tag{A.1}$$

Here, the symbols include the following relations:

$$\begin{aligned}
 d_{11} &= a_{11,1} e_{11} + a_{12,1} e_{21}, \quad d_{12} = a_{11,1} e_{12} + a_{12,1} e_{22}, \quad d_{13} = a_{11,1} e_{13} + a_{12,1} e_{23} + a_{112} \\
 d_{14} &= a_{11,1} e_{14} + a_{12,1} e_{24} + a_{12,2}, \quad d_{15} = a_{11,1} e_{15} + a_{12,1} e_{25} + a_{15,1}, \quad d_{18} = a_{11,1} e_{18} + a_{12,1} e_{28} + a_{18,1}, \\
 d_{21} &= a_{21,1} e_{11} + a_{22,1} e_{21}, \quad d_{22} = a_{21,1} e_{12} + a_{22,1} e_{22}, \quad d_{23} = a_{21,1} e_{13} + a_{22,1} e_{23} + a_{212}, \\
 d_{24} &= a_{21,1} e_{14} + a_{22,1} e_{24} + a_{22,2}, \quad d_{25} = a_{21,1} e_{15} + a_{22,1} e_{25} + a_{25,1}, \quad d_{28} = a_{21,1} e_{18} + a_{22,1} e_{28} + a_{28,1}, \\
 d_{31} &= a_{66,1} e_{31}, \quad d_{32} = a_{66,1} e_{32} + 2a_{66,2}, \quad d_{35} = a_{35,1} - a_{66,1} e_{35}, \quad d_{38} = a_{38,1} - a_{66,1} b_{38}, \\
 \delta_{i+2} &= \int_{-h/2}^{h/2} \frac{df_i(z_i)}{dz} dz \quad (i=1,2).
 \end{aligned} \tag{A.2}$$

where



$$\begin{aligned}
 e_{11} &= \frac{a_{22,0}}{a_{11,0}a_{22,0} - a_{12,0}a_{21,0}}, e_{12} = -\frac{a_{12,0}}{a_{11,0}a_{22,0} - a_{12,0}a_{21,0}}, e_{13} = \frac{a_{12,0}a_{21,1} - a_{11,1}a_{22,0}}{a_{11,0}a_{22,0} - a_{12,0}a_{21,0}}, \\
 e_{14} &= \frac{a_{12,0}a_{22,1} - a_{12,1}a_{22,0}}{a_{11,0}a_{22,0} - a_{12,0}a_{21,0}}, e_{15} = \frac{a_{25,0}a_{12,0} - a_{15,0}a_{22,0}}{a_{11,0}a_{22,0} - a_{12,0}a_{21,0}}, e_{18} = \frac{a_{28,0}a_{12,0} - a_{18,0}a_{22,0}}{a_{11,0}a_{22,0} - a_{12,0}a_{21,0}}, \\
 e_{21} &= -\frac{a_{21,0}}{a_{11,0}a_{22,0} - a_{12,0}a_{21,0}}, e_{22} = \frac{a_{11,0}}{a_{11,0}a_{22,0} - a_{12,0}a_{21,0}}, e_{23} = \frac{a_{11,1}a_{21,0} - a_{21,1}a_{11,0}}{a_{11,0}a_{22,0} - a_{12,0}a_{21,0}}, \\
 e_{24} &= \frac{a_{12,1}a_{21,0} - a_{22,1}a_{11,0}}{a_{11,0}a_{22,0} - a_{12,0}a_{21,0}}, e_{25} = \frac{a_{15,0}a_{21,0} - a_{25,0}a_{11,0}}{a_{11,0}a_{22,0} - a_{12,0}a_{21,0}}, e_{28} = \frac{a_{18,0}a_{21,0} - a_{28,0}a_{11,0}}{a_{11,0}a_{22,0} - a_{12,0}a_{21,0}}, \\
 e_{31} &= \frac{1}{a_{66,0}}, b_{32} = -\frac{2a_{66,1}}{a_{66,0}}, e_{35} = \frac{a_{35,0}}{a_{66,0}}, e_{38} = \frac{a_{38,0}}{a_{66,0}}
 \end{aligned} \tag{A.3}$$

in which

$$\begin{aligned}
 a_{11,i} &= \int_{-h/2}^{h/2} Q_{11}(z_1, T)z^i dz, a_{22,i} = \int_{-h/2}^{h/2} Q_{22}(z_1, T)z^i dz, A_{12,i} = \int_{-h/2}^{h/2} Q_{12}(z_1, T)z^i dz = \int_{-h/2}^{h/2} Q_{21}(z_1, T)z^i dz = a_{21,i}, \\
 a_{66,i} &= \int_{-h/2}^{h/2} Q_{66}(z_1, T)z^i dz, i = 0, 1, 2. a_{15,i_1} = \int_{-h/2}^{h/2} \delta_1 Q_{11}(z_1, T)z^{i_1} dz, a_{18,i_1} = \int_{-h/2}^{h/2} \delta_2 Q_{12}(z_1, T)z^{i_1} dz, \\
 a_{25,i_1} &= \int_{-h/2}^{h/2} \delta_1 Q_{21}(z_1, T)z^{i_1} dz, a_{28,i_1} = \int_{-h/2}^{h/2} \delta_2 Q_{22}(z_1, T)z^{i_1} dz, a_{35,i_1} = \int_{-h/2}^{h/2} \delta_1 Q_{66}(z_1, T)z^{i_1} dz, \\
 a_{38,i_1} &= \int_{-h/2}^{h/2} \delta_1 Q_{66}(z_1, T)z^{i_1} dz, i_1 = 0, 1.
 \end{aligned} \tag{A.4}$$

Appendix B

Here \mathbb{L}_{ij} are differential operators and defined as:





$$\begin{aligned}
 \mathbb{L}_{11}F &= d_{12} \frac{\partial^4}{\partial X^4} + (d_{11} - 2d_{31} + d_{22}) \frac{\partial^4}{\partial X^2 \partial Y^2} + d_{21} \frac{\partial^4}{\partial Y^4} \\
 \mathbb{L}_{12}w &= -d_{13} \frac{\partial^4}{\partial X^4} - (d_{14} + 2d_{32} + d_{23}) \frac{\partial^4}{\partial X^2 \partial Y^2} - d_{24} \frac{\partial^4}{\partial Y^4} - N_1 \frac{\partial^2}{\partial X^2} - N_2 \frac{\partial^2}{\partial Y^2} + k_1 \\
 \mathbb{L}_{21}F &= e_{22} \frac{\partial^4}{\partial X^4} + (e_{12} + e_{31} + e_{21}) \frac{\partial^4}{\partial X^2 \partial Y^2} + e_{11} \frac{\partial^4}{\partial Y^4} \\
 \mathbb{L}_{22}w &= -e_{23} \frac{\partial^4}{\partial X^4} - (e_{13} - e_{32} + e_{24}) \frac{\partial^4}{\partial X^2 \partial Y^2} - e_{14} \frac{\partial^4}{\partial Y^4}
 \end{aligned} \tag{B.1}$$

Appendix C

Here r_{ij} are described as:

$$\begin{aligned}
 r_{11} &= [(d_{11} - d_{31})q^2 + c_{12}p^2]p^2h, r_{12} = [(d_{14} + d_{32})q^2 + d_{13}p^2]p^2, r_{13} = [d_{15}p^2 + d_{35}q^2 + \delta_3]p, \\
 r_{14} &= (d_{18} + d_{38})qp^2, r_{21} = [d_{21}q^2 + (d_{22} - d_{31})p^2]q^2h, r_{22} = [(d_{32} + d_{23})p^2 + d_{24}q^2]q^2, \\
 r_{23} &= (d_{25} + d_{35})pq^2, r_{24} = [d_{28}q^2 + d_{38}p^2 + \delta_4]q, r_{31} = [e_{22}p^4 + (e_{12} + e_{21} + e_{31})p^2q^2 + e_{11}q^4]h, \\
 r_{32} &= e_{23}p^4 + (e_{24} + e_{13} + e_{32})p^2q^2 + e_{14}q^4, r_{33} = [e_{25}p^2 + (e_{15} + e_{35})q^2]p, \\
 r_{34} &= q[(e_{28} + e_{38})p^2 + e_{18}q^2], r_{41} = 0, \bar{r}_{42} = N_1p^2 + N_2q^2 - r_w, r_w = K_w, r_{43} = \delta_3p, r_{44} = \delta_4q.
 \end{aligned} \tag{C.1}$$

ORCID iD

Cengiz Ipek  <https://orcid.org/0000-0001-5319-1048>
 Abdullah H. Sofiyev  <https://orcid.org/0000-0001-7678-6351>
 Nicholas Fantuzzi  <https://orcid.org/0000-0002-8406-4882>
 Sadige P. Efendiyeva  <https://orcid.org/0000-0003-4960-0616>



© 2023 Shahid Chamran University of Ahvaz, Ahvaz, Iran. This article is an open access article distributed under the terms and conditions of the Creative Commons Attribution-NonCommercial 4.0 International (CC BY-NC 4.0 license) (<http://creativecommons.org/licenses/by-nc/4.0/>).

How to cite this article: Ipek C., Sofiyev A.H., Fantuzzi N., Efendiyeva S.P. Buckling Behavior of Nanocomposite Plates with Functionally Graded Properties under Compressive Loads in Elastic and Thermal Environments, *J. Appl. Comput. Mech.*, 9(4), 2023, 974–986. <https://doi.org/10.22055/jacm.2023.43091.4019>

Publisher’s Note Shahid Chamran University of Ahvaz remains neutral with regard to jurisdictional claims in published maps and institutional affiliations.

